Title: Linking Arctic variability and change with extreme winter weather in the US

Authors: Judah Cohen[1,2*], Laurie Agel[3], Mathew Barlow[3], Chaim Garfinkel[4] and Ian White[4]

Affiliations:

[1]Atmospheric and Environmental Research, Inc., Lexington, Massachusetts 02421, USA.

[2]Department of Civil and Environmental Engineering, Massachusetts Institute of Technology, Cambridge, MA, 02139, USA.

[3]Department of Environmental, Earth, and Atmospheric Sciences, University of Massachusetts Lowell, Lowell, MA, USA.

[4]The Hebrew University of Jerusalem, Institute of Earth Sciences, Edmond J. Safra Campus, Jerusalem, Israel.

*Corresponding author. Email: jcohen@aer.com

Abstract: The Arctic is warming at a rate twice the global average and severe winter weather is reported to be increasing across many heavily populated mid-latitude regions, but there isn't yet agreement on whether there is a physical link between the two phenomena. Here we use observational analysis to show that a lesser-known stratospheric polar vortex (SPV) disruption that involves wave reflection and stretching of the SPV is linked with extreme cold across parts of Asia and North America, including the recent February 2021 Texas cold wave, and has been increasing over the satellite era. We then use numerical modeling experiments forced with trends in autumn snow cover and Arctic sea ice to establish a physical link between Arctic change and SPV stretching and surface impacts.

Summary: We show that Arctic change is likely contributing to the observed increasing trend of polar vortex stretching associated with extreme cold in Asia and the US.

Main Text: Anthropogenic global warming is projected to increase some weather extremes—for example more heat waves and heavy precipitation events (*1, 2*)—but not severe winter weather such as cold air outbreaks and heavy snowfalls (*3, 4*). Yet contrary to global climate model projections, recent weather extremes have included an increase in cold air outbreaks and/or heavy snowfalls across the Northern Hemisphere (NH) since 1990 up to the recent past (*5, 6, 3, 7, 8*). The most recent example of extreme winter weather was the anomalous cold weather of January and February 2021 in Asia (*9*), Europe (*10, 11*) and especially the United States (US). The US Southern Plains cold wave of February 2021 may be unique in the observational record for the region based on the aggregate severity of the cold intensity, cold duration and widespread disruptive snowfall (*12, 13*). The collapse of the Texas energy infrastructure could make it the state's costliest natural disaster, even more so than previous hurricanes (*14*) and at least two to three times costlier than the entire record-breaking North Atlantic 2020 hurricane season (*15*). This event has reignited the debate whether climate change contributes to more severe winter weather (*16*).

One of the more robust signatures of global warming is accelerated Arctic warming, known as Arctic Amplification (AA) (*17*), and has been evident since the 1990s (*5*). AA is both a response to and accelerator of Arctic sea ice decline, with the greatest losses observed in the Barents-Kara and Chukchi-Bering Seas in the fall and winter (*8*). AA has also coincided with increasing snow fall/cover at high latitudes including across Eurasia during October through January (*18–20*), in part due to the decline in sea ice, which increases moisture availability in the Arctic (*18, 20*). In Figs. S1 and S2, we show that Eurasian October snow cover has increased, while fall Arctic sea ice has decreased over the satellite and AA periods.

An hypothesis that has received much recent attention is that AA is driving winter mid-latitude cooling (*7, 22, 23*). One theory that links less sea ice and/or more Eurasian snow cover to severe winter weather in the mid-latitudes involves a pathway through the SPV (*5, 24*). Less sea ice and more snow cover increase the probability of a stronger Siberian high-pressure ridge and upward atmospheric wave energy flux. Increased wave flux from the troposphere to the stratosphere can result in a sudden stratospheric warming (SSW) characterized by large rises in polar geopotential heights centered over the North Pole, often followed by an increase in NH severe winter weather (*3*). However, whether AA can result in more severe winter weather, and how, is a matter of active debate.

Kretschmer et al. (*30*) used a machine learning (ML) technique to demonstrate that the weakest SPV state (SSWs) are increasing in frequency while the strongest SPV states are decreasing in January and February over the period of AA. In a follow up study, the same ML technique identified a less-known SPV disruption where the SPV is stretched (*31*) (P4 in Fig. 1) as opposed to the well-known SSW (P5 in Fig. 1). One important difference between SSWs and SPV stretching is that the vertical component of atmospheric wave energy known as wave activity flux (WAF_z) or Eliassen Palm (EP) flux preceding SSWs converges in the polar stratosphere resulting in rapid warming and rising of geopotential heights in the stratosphere, while during SPV stretching, WAF_z is reflected from the SPV back into the troposphere (and are therefore also referred to as "reflective" events) (*32–34*) where it amplifies the climatological pressure ridge and trough across North America. A second important difference is that North American cold spells tend to be more extreme following SPV stretching events (*31*).

Here we expand the analysis of SPV variability and its tropospheric links to include fall and early winter, which identifies trends and links to surface snow and ice changes in the high latitudes which are consistent with surface forcing of the SPV variability. We then use modeling experiments to establish a causal link between the surface changes and the SPV variability and its tropospheric links and, therefore, between AA and extreme mid-latitude winter weather.

We extend the ML technique of Kretschmer et al.(*30, 31*) to analyze SPV variability in fall and early winter (October through December) over the reanalysis period (1980 through early 2021), shown in Fig. 1 (in Fig. S3 we update Kretschmer et al. (*31*) January and February analysis). The first two clusters (P1 and P2 in Fig. 1) show a stronger than normal SPV (i.e., lower geopotential heights), and the last two (P4 and P5) show a weaker than normal SPV (i.e., higher geopotential heights in the polar stratosphere). The stronger SPV states are experiencing a statistically significant decreasing trend in frequency while the weaker SPV states are experiencing a statistically significant increasing trend, not only for January and February but also for the preceding months of October through December (Fig. S4). Here we show for the first time that SPV stretching disruptions (P4) have a statistically significant increasing trend in both fall and winter, even more so than SSWs over the reanalysis period, and are increasing for the months October through February (Fig. S5).

The concurrent surface temperature anomalies are presented in Fig. 1e. The two strong SPV states exhibit a cold Arctic/warm continent pattern and the two weak SPV states exhibit a warm Arctic/cold continent pattern. Specifically, for the two weak states, SSWs (P5) are related to warming around Greenland and Baffin Bay while SPV stretching (P4) is related to Arctic warming focused in the Barents-Kara and Chukchi-Bering Seas. In the mid-latitudes, both SSWs and SPV stretching are associated with relatively cold temperatures across Northern Europe, Northern and Eastern Asia and North America; however, during SPV stretching, North American cold temperatures are more widespread and shifted eastward. It has already been shown that SSWs are contributing to an observed cooling trend across northern Eurasia for the two winter months of January and February (*30, 35*) but our analysis suggests that an increasing number of SPV stretching events are a cooling influence across North America.

The tropospheric precursor pattern to SSWs has been previously identified as consisting of relatively high pressure across Northern Europe and the Urals coupled with relatively low pressure across East Asia into the northern North Pacific (*30*, *36, 37*). This anomalous dipole projects onto the climatological standing wave-1 of the NH (*36–38*), and through constructive interference gives rise to an enhanced WAF_z from the troposphere to the stratosphere. Although anomalous vertical wave energy flux has also been shown to precede SPV stretching disruptions (*31*), other precursor features in the tropospheric circulation to these events have not yet been examined.

The precursor patterns to SPV stretching events are shown in Fig. 2. At 100 hPa in the lower stratosphere (Fig. 2a) there are regional ridging/positive height anomalies, which begin over the North Atlantic then migrate to the Gulf of Alaska, Alaska, Chukchi-Barents-Kara Seas and the Urals. The ridging amplifies shortly before and up until the time of the event (day 0). In addition, prior to SPV stretching there is a WAF_z dipole (Fig. 2b) with positive anomalies in Eastern Siberia and negative anomalies in northwest North America (similar to Kretschmer et al.) (*29*). Climatologically, WAF_z is upward over Siberia, reflected in the stratosphere, and then downward over Canada (*29*). The low and mid-troposphere precursor patterns (Figs. 2c-d) project onto the climatological NH standing wave-2 (*36, 37*). Finally, the observed precursors in surface temperature (Fig. 2e) begin as positive anomalies in the Arctic focused near Greenland and to a lesser extent in the Chukchi Sea. However shortly before and at the time of the event, two regions of positive anomalies emerge—one over the North Atlantic side of the Arctic and a second over Alaska and Chukchi-Bering Seas region of even greater amplitude and extent, while negative temperature anomalies emerge first in Siberia but then also develop over North America.

Could climate change have contributed to the observed increasing trends in the SPV stretching events that force cold to extreme cold in North America and East Asia? In Fig. 3, we show the trends (1980–2021) in the late fall and winter months of the same variables used to identify the precursors to SPV stretching events. Trends in lower stratospheric WAF_z exhibit the same dipole associated with SPV stretching events with positive trends over Siberia and negative trends over northwest North America (10-0 days previous; Fig. 2b). At the surface and 500-hPa mid-to-high latitudes, increasing trends in pressure/geopotential heights are centered on the Barents-Kara Seas and Urals with a secondary maximum in the Gulf of Alaska and Alaska region, which matches what is observed in the precursors to SPV stretching (15-0 days previous Fig. 2c-d). Surface temperatures have been rising most strongly in the Arctic with two maximum centers, one in the North Atlantic side of the Arctic and the other in the Chukchi-Bering Seas similar to the observed Arctic warming prior to SPV stretching events (15-0 days previous Fig. 2e). There is some weak cooling in Asia. Projections of the seasonal and monthly (October through February) SPV stretching precursors (see Figs. 3a and S6), onto the trends are statistically significant (see Figs. S7 and S8), especially relatively warm surface temperatures in the Barents-Kara and Chukchi-Bering Seas, ridging/high pressure at 500 hPa and at the surface in the Barents-Kara Seas/Urals and to a lesser extent, the northern North Pacific.

We complete our observational analysis by correlating leading Eurasian snow cover and Arctic sea ice concentration with the lagging atmospheric fields analyzed for trends (Fig. 3b and 3c; with all time-series detrended). The correlations with snow cover (Fig. 3b) most closely resemble SPV stretching precursors (Fig. 2), with ridging centered near Alaska and downstream troughing over eastern North America and into the North Atlantic and Europe (the correlation between snow and SPV stretching frequency is statistically significant). In contrast, correlations with Barents-Kara sea ice (Fig. 3c) most closely resemble the observed trends, especially the pan-Arctic geopotential height rises in the lower stratosphere (100-hPa) and pressure ridging from the Urals to Greenland at 500 hPa (correlations between ice with SSW frequency and ice with SPV stretching frequency are both found to be significant), more reminiscent of the atmospheric response to SSWs (Fig. 1c for P5). Despite the statistically significant correlations, it is a challenge to demonstrate cause and effect with observational analysis alone.

To more directly assess the physical links, we conducted numerical modeling experiments related to both increased Eurasian snow cover and reduced sea ice, using a simplified global climate model (GCM). This kind of model is well-suited for isolating the atmospheric response to idealized heating perturbations (*39*) (see Methods).

To simulate the observed trend of more extensive October Eurasian snow cover (Fig. S2), the model was forced with increased surface albedo (Fig. S9). About two months after the forcing switch-on, the model response shows features that resemble the circulation anomalies associated with SPV stretching events, including a stretched SPV, the lower stratospheric dipole in poleward heat transport (a good proxy for WAF_z), and the mid-troposphere ridging/warm anomalies in Alaska and the Bering Sea, and troughing/cool anomalies in East Asia and eastern North America (see Fig. 4b and Fig. S10b for comparison with the stretched SPV pattern from cluster analysis in Fig. 2). The simulated atmospheric response to snow cover forcing is of comparable magnitude to the atmospheric response inferred from observational analysis (Fig. 4a), though in many previous GCM snow sensitivity experiments the simulated response is weaker (*40*).

Since Barents-Kara sea ice shows a strong observational relationship with Ural mid-tropospheric ridging and downstream East Asian troughing (Fig. 3c) that projects strongly onto the precursor pattern of SPV stretching events (Fig. 2c), we further forced the GCM with anomalous heating in the Barents-Kara Seas during October through December where ice loss is observed (Figs. S2 and S9). The simulated atmospheric response to both snow and ice forcing (Fig. 4d) exhibits a similar pattern to the correlations between sea ice with ridging/warming centered in the Barents-Kara Seas at 100, 500 and 850-hPa and troughing/cooling in East Asia in the mid to low troposphere (Fig. 3c). In addition, the model forced with both snow and ice anomalies includes ridging/warming in the Chukchi-Bering seas at 500 and 850-hPa and accelerates the model response to Arctic changes by about a month. The simulated atmospheric response to the combined forcing of snow and ice is of comparable magnitude but somewhat weaker than the inferred response from observational analysis but still larger than many previous GCM studies (*3, 41*).

We also examine the regression of Eurasian snow cover (Fig. 4a) and multiple regression of snow and Barents-Kara sea ice (Fig. 4c) with the atmospheric circulation. Correlations with snow cover exhibit ridging/warming focused on the North Pacific side of the Arctic from the surface to the lower stratosphere. Therefore, the atmospheric response to snowcover-only forcing better matches the atmospheric anomalies associated with SPV stretching events than the atmospheric response to sea-ice-only forcing, where the ridging/warming is either focused in the Barents-Kara seas or is pan-Arctic. However, when including both snow and ice, the atmospheric response in both observations and in the model better matches full Arctic trends, and the model atmospheric response of SPV stretching is more persistent, with troughing/cold temperatures in North America persisting for more than three weeks (days 36–60, see Fig. S11). Both observational analysis and modeling experiments show that Chukchi-Bering sea ice loss has little impact on the SPV consistent with previous studies (*42*), however the tropospheric response to Chukchi-Bering sea ice loss can amplify (based on observations, Fig. S12) or force Alaska ridging/warming and downstream North American troughing/cooling (Fig. S13). Although Chukchi-Bering sea ice loss may not force SPV disruptions, it could amplify the tropospheric response across Asia and North America (*43*).

Finally, we examined the relationship between reflective/stretching SPV events and the past winter. We applied our clustering technique to observed 100-hPa geopotential heights in January and February 2021. Though our analysis shows January 2021 was dominated by P5, it identifies P4 for over 60% of the days from January 29^{th} through February 15^{th}. Also, in early February WAF_z was upward over Siberia and downward over Canada, consistent with SPV stretching events, as opposed to convergence in the stratosphere (consistent with SSW events), as observed in early January prior to an SSW on January 5^{th} (see Fig. S14). Though the SSW observed in January may have also contributed to the hemispheric pattern in February, our analysis supports that the historic February (approximately 6th–21st) 2021 Texas cold wave was likely the response to the SPV stretching in February and the atmospheric circulation can be seen transitioning from circulation anomalies associated with SSWs to those associated with SPV stretching from late January through early February (see Fig. S15).

In this analysis, we have demonstrated that SPV stretching events have accelerated in the era of AA. Climate change in general, but Arctic change in particular, is favorable for forcing these events. In Fig. S16 we provide a generalized timeline of the significant atmospheric features beginning with Ural ridging, followed by North Pacific ridging and ending with North American and East Asian cold. It is argued that warming in the Barents-Kara and Chukchi-Bering Seas favor ridging/high pressure in these regions in the troposphere (*3, 8, 43*). Autumn Siberian snowfall has also been increasing (*21*), favoring troughing over East Asia. This pattern of ridging in the Urals/Barents-Kara Seas region and troughing in East Asia strongly projects onto the tropospheric pattern favorable for forcing SPV stretching that often delivers extreme cold to Canada and the US. This interpretation is supported by a GCM forced with increased Eurasian snow cover and decreased Barents-Kara sea ice, where the atmospheric response is an increase in SPV stretching events with troughing and colder temperatures across Asia and North America one to two months following the introduction of Arctic forcing. Therefore, Arctic change is likely contributing to the increasing frequency of SPV stretching events including one just prior to the Texas cold wave of February 2021.

These results have important societal implications. First, they highlight an important type of stratosphere-troposphere coupling, SPV stretching, that has been mostly hidden in the heretofore principal focus on SSWs, even though the impact of SPV stretching events on North American temperatures can be of greater extent and magnitude (*31*). Second, the identification of the precursor pattern to stretching events can potentially extend the warning lead time of cold extremes in Asia, Canada and the US. Third, our analysis is informative for policy makers. Preparing for only a decrease in severe winter weather can compound the human and economic cost when severe winter weather does occur, as exemplified during the Texas cold wave of February 2021.

References and Notes

1. D. Coumou, S. Rahmstorf, A decade of weather extremes. *Nat. Clim. Change* **2**, 491–496 (2012).
2. D. Coumou, J. Lehmann, J. Beckmann, The weakening summer circulation in the Northern Hemisphere mid-latitudes. *Science* **17**, 324–327 (2015).
3. J. Cohen, X. Zhang, J. Francis, T. Jung, R. Kwok, J. Overland, T. Ballinger, U.S. Bhatt, H. W. Chen, D. Coumou, S. Feldstein, H. Gu, D. Handorf, G. Henderson, M. Ionita, M. Kretschmer, F. Laliberte, S. Lee, H. W. Linderholm, W. Maslowski, Y. Peings, K. Pfeiffer, I. Rigor, T. Semmler, J. Stroeve, P.C. Taylor, S. Vavrus, T. Vihma, S. Wang, M. Wendisch, Y. Wu, J. Yoon, Divergent consensuses on Arctic amplification influence on mid-latitude severe winter weather. *Nature Clim. Change* **10,** 20–29 (2020).

4. W. S. Ashley, A. M. Haberlie, V. A. Gensini, Reduced frequency and size of late-twenty-first-century snowstorms over North America. *Nature Clim. Change* **10,** 539–544 (2020). Doi: 10.1038/s41558-020-0774-4
5. J. Cohen, J. A. Screen, J. C. Furtado, M. Barlow, D. Whittleston, D. Coumou, J. Francis, K. Dethloff, D. Entekhabi, J. Overland, J. Jones, Recent Arctic amplification and extreme mid-latitude weather. *Nature Geosci*. **7**(9), 627–637 (2014).
6. J. Cohen, K. Pfeiffer, J. Francis, Warm Arctic episodes linked with increased frequency of extreme winter weather in the United States. *Nat. Commun.* **9**(869) (2018). doi: 10.1038/s41467-018-02992-9
7. J. E. Overland, J. Francis, R. Hall, E. Hanna, S.-J. Kim, T. Vihma, The melting Arctic and mid-latitude weather patterns: Are they connected? *J. Clim.***28**, 7917–7932 (2015).
8. J. E. Overland, T. J. Ballinger, J. Cohen, J. A. Francis, E. Hanna, R. Jaiser, B.-M. Kim S.-J. Kim, M. Kretschmer, J. Ukita, T. Vihma, M. Wang, X. Zhang, How do intermittency and simultaneous processes obfuscate the Arctic influence on midlatitude winter extreme weather events? *Environ. Res. Lett.***16**, 043002 (2021).

9. F. Zheng, Y. Yuan, Y. Ding, K. Li, X. Fang, Y. Zhao, Y. Sun, J. Zhu, Z. Ke, J. Wang, X Jia, The 2020/21 extremely cold winter in China influenced by the synergistic effect of La Niña and warm Arctic. *Adv. Atmos. Sci.* (2021). doi: 10.1007/s00376-021-1033-y

10. https://www.euronews.com/2021/01/07/spain-records-coldest-ever-temperature-at-35-8-c
11. https://www.dw.com/en/german-village-logs-289-celsius-overnight-as-cold-snap-persists/a-56576765
12. https://twitter.com/capitalweather/status/1364681912728621057 and https://www.washingtonpost.com/weather/2021/02/24/texas-winter-storm-temperature-records/?arc404=true
13. J. Doss-Gollin, D. J. Farnham, U. Lall, V. Modi, How unprecedented was the February 2021 Texas cold snap. *Env. Res. Lett.* **16**, 064056 (2021).
14. https://www.texastribune.org/2021/02/25/texas-winter-storm-cost-budget/
15. https://www.accuweather.com/en/winter-weather/damages-from-feb-snowstorms-could-be-as-high-as-155b/909620
16. https://www.nytimes.com/2021/02/18/briefing/texas-blackouts-mars-rover-cuomo-new-york.html
17. M. Serreze, A. Barrett, J. Stroeve, D. Kindig, M. Holland, The emergence of surface based Arctic amplification. *Cryosphere* **3,** 11–19 (2009).
18. J. Cohen, J. Jones, J. C. Furtado, E. Tziperman, Warm Arctic, cold continents: A common pattern related to Arctic sea ice melt, snow advance, and extreme winter weather. *Oceanogr.* **26**, 150–160 (2013).
19. M. Wegmann, M. Roher, M. Santolaria-Otín, G. Lohmann, Eurasian autumn snow link to winter North Atlantic Oscillation is strongest for Arctic warming periods. *Earth Syst. Dynam.* **11**, 509–524 (2020). doi: 10.5194/esd-11-509-2020.

20. Z. Lü, F. Li, Y. J. Orsolini, Y. Gao, S. He, Understanding of European cold extremes, sudden stratospheric warming, and Siberian snow accumulation in the winter of 2017/18. *J. Clim.* **33**, 527-545 (2020). doi: 10.1175/JCLI-D-18-0861.1
21. M. Wegmann, Y. Orsolini, M. Vázquez, L. Gimeno, R. Nieto, O. Bulygina, R. Jaiser, D. Handorf, A. Rinke, K. Dethloff, Arctic moisture source for Eurasian snow cover variations in autumn. *Environ. Res. Lett.* **10**, 054015 (2015).
22. T. Vihma, Effects of Arctic sea ice decline on weather and climate: a review. *Surv. Geophys.* **35**, 1175–1214 (2014). doi: 10.1007/s10712-014-9284-0
23. R. L. Newson, Response of a general circulation model of the atmosphere to removal of the Arctic ice-cap. *Nature* **241**, 39–40 (1973).
24. J. Zhang, W. Tian, M. Chipperfield, F. Xie, J. Huang, Persistent shift of the Arctic polar vortex towards the Eurasian continent in recent decades. *Nature Clim. Change* **6,** 1094–1099 (2016). Doi: 10.1038/nclimate3136
25. E. Kintisch, Into the maelstrom. *Science* **344**, 250 (2014).
26. C. Gramling, Arctic impact. *Science* **347**, 818–821 (2015).
27. J. M. Wallace, I. M. Held, D. W. J.Thompson, K. E.Trenberth, J. E.Walsh, Global warming and winter weather. *Science* **343**, 729–730 (2014).
28. T. G. Shepherd, Effects of a warming Arctic. *Science* **353**, 989–990 (2016).
29. R. J. Blackport, A. Screen, K. van der Wiel, R. Bintanja, Minimal influence of reduced Arctic sea ice on coincident cold winters in mid-latitudes. *Nature Clim. Change.* **9**, 697–704 (2019). doi: 10.1038/s41558-019-0551-4

30. M. Kretschmer, D. Coumou, L. Angel, M. Barlow, E. Tziperman, J. Cohen, 2018a: More persistent weak stratospheric polar vortex states linked to mid-latitude cold extremes, *Bull. Am. Meteorol. Soc.* **99**(1) 49–60 (2018a). doi.org/10.1175/BAMS-D-16-0259.1

31. M. Kretschmer, J. Cohen, V. Matthias, J. Runge, D. Coumou, The different stratospheric influences on cold extremes in northern Eurasia and North America, *npj Clim. Atmos. Sci.* **1**(1), 1–10 (2018b). doi: 10.1038/s41612-018-0054-4

32. K. Kodera, H. Mukougawa, S. Itoh, Tropospheric impact of reflected planetary waves from the stratosphere. *Geophys. Res. Lett.***35,** L16806 (2008).

33. K. Kodera, H. Mukougawa, A. Fujii, Influence of the vertical and zonal propagation of stratospheric planetary waves on tropospheric blockings. *J. Geophys. Res. Atmos.* **118,** 8333–8345 (2013).

34. D. Nath, W. Chen, L. Wang, Y. Ma, Planetary wave reflection and its impact on tropospheric cold weather over Asia during January 2008. *Adv. Atmos. Sci.*, **31**, 851–862 (2014). doi: 10.1007/s00376-013-3195-8

35. C. I. Garfinkel, S. W. Son, K. Song, V. Aquila, L. D. Oman, Stratospheric variability contributed to and sustained the recent hiatus in Eurasian winter warming. *Geophys. Res. Lett.* **44**(1), 374–382 (2017).

36. O. Martius, L. M.Polvani, H. C.Davies, Blocking precursors to stratospheric sudden warming events. *Geophys. Res. Lett.* **36**(14), L14806 (2009). doi: 10.1029/2009GL038776

37. C. Garfinkel, D. Hartmann, F. Sassi, Tropospheric precursors of anomalous Northern Hemisphere stratospheric polar vortices. *J. Clim.* **23**, 3282–3299 (2020).

38. K. Smith, P. J. Kushner, J. Cohen, The role of linear interference in Northern Annular Mode variability associated with Eurasian snow cover extent, *J. Clim.* **24**, 6185–6202 (2011).

39. P. Maher, E. P. Gerber, B. Medeiros, T. M. Merlis, S. Sherwood, A. Sheshadri, et al., Model hierarchies for understanding atmospheric circulation, *Rev. Geophys.*, **57,** 250–280 (2019). doi: 10.1029/2018RG000607.

40. G. R. Henderson, Y. Peings, J. C. Furtado, P. J. Kushner, Snow-atmosphere coupling in the Northern Hemisphere, *Nature Clim. Change* **8,** 954–963 (2018) doi: 10.1038/s41558-018-0295-6)

41. M. Kretschmer, G. Zappa, T. G. Shepherd, The role of Barents and Kara sea ice loss in projected polar vortex changes, *Weather Clim. Dynam.* **1**, 715–730 (2020).

42. C. M. McKenna, T. J. Bracegirdle, E. F. Shuckburgh, P. H. Haynes, M. M. Joshi, Arctic sea-ice loss in different regions leads to contrasting Northern Hemisphere impacts. *Geophys. Res. Lett.* **44** (2017). doi: 0.1002/2017GL076433

43. J.-S. Kug, J. H. Jeong, Y. S. Jang, B.-M. Kim, C. K. Folland, S.-K. Min, S.-W. Son, Two distinct influences of Arctic warming on cold winters over North America and East Asia. *Nature Geosci.* **8**, 759–762 (2015). doi: 10.1038/ngeo2517

44. R. Gelaro, W. MaCarty, M. J. Suarez, R. Todling, A. Molod, L. Takacs, C. A. Randles, A. Darmenov, M. G. Bosilovich, R. Reichle, K. Wargan, L. Coy, R. Cullather, C. Draper, S. Akella, V. Buchard, A. Conaty, A. M. da Silva, W. Gu, G.-K. Kim, R. Koster, R. Lucchesi, D. Merkova, J. E. Nielsen, G. Partyka, S. Pawson, W. Putman, M. Reinecker, S. D. Schubert, M. Sienkiewicz, B. Zhao, The Modern-Era Retrospective Analysis for Research and Applications, Version 2 (MERRA-2), *J. Clim.* **30**, 5419–5454 (2017).

45. Global Modeling and Assimilation Office (GMAO), MERRA-2 inst3_3d_asm_Np: 3d, 3-Hourly, Instantaneous, Pressure-Level, Assimilation, Assimilated Meteorological Fields V5.12.4, Greenbelt, MD, USA, Goddard Earth Sciences Data and Information Services Center (GES DISC), Accessed: [*Mar 15, 2021*], (2015a). doi: 10.5067/QBZ6MG944HW0

46. Global Modeling and Assimilation Office (GMAO), MERRA-2 inst1_2d_asm_Nx: 2d, 1-Hourly, Instantaneous, Single-Level, Assimilation, Single-Level Diagnostics V5.12.4, Greenbelt, MD, USA, Goddard Earth Sciences Data and Information Services Center (GES DISC), Accessed: [*Mar 15, 2021*], (2015b). doi: 10.5067/3Z173KIE2TPD

47. R. A. Plumb, On the three-dimensional propagation of stationary waves. *J. Atmos. Sci.* **42**(3), 217– 229 (1985).

48. D. A. Robinson, T. W. Estilow, NOAA CDR Program, NOAA Climate Data Record (CDR) of Northern Hemisphere (NH) Snow Cover Extent (SCE), Version 1. [version 4]. NOAA National Centers for Environmental Information (2012). doi: 10.7289/V5N014G9

49. N. A. Rayner, D. E. Parker, E. B. Horton, C. K. Folland, L. V. Alexander, D. P. Rowell, E. C. Kent, A. Kaplan, Global analyses of sea surface temperature, sea ice, and night marine air temperature since the late nineteenth century. *J. Geophys. Res.* **108**, D14, 4407 (2003). doi: 10.1029/2002JD002670

50. J. Cohen, M. Barlow, P. Kushner, K. Saito, 2007: Stratosphere-Troposphere coupling and links with Eurasian Land-Surface Variability, *J. Climate*, **20**, 5335–5343 (2007).

51. M. Honda, J. Inoue, S, Yamane, Influence of low Arctic sea-ice minima on anomalously cold Eurasian winters. *Geophys. Res. Lett.* **36**, (2009). doi: 10.1029/2008GL037079

52. B.-M. Kim, S.-W. Son, S.-K. Min, J.H. Jeong, S.-J. Kim, X. Zhang, T. Shim, J.-H. Yoon, Weakening of the stratospheric polar vortex by Arctic sea-ice loss. *Nature Comm.* **5**, (2014). doi:10.1038/ncomms5646

53. P. Zhang, Y. Wu, I. R. Simpson, K. L. Smith, X. Zhang, B. De, P. Callaghan, A stratospheric pathway linking a colder Siberia to Barents-Kara sea ice loss. *Sci. Adv.* **4**, eaat6025 (2018).

54. M. Jucker, E. Gerber, Untangling the annual cycle of the tropical tropopause layer with an idealized moist model. *J. Clim.* **30**(18), 7339–7358 (2017).

55. C. I. Garfinkel, I. White, E. P. Gerber, M. Jucker, The impact of SST biases in the tropical East Pacific and Agulhas current region on atmospheric stationary waves in the southern hemisphere. *J. Clim.* **33**(21), 9351–9374 (2020).

56. C. I. Garfinkel, I. P. White, E. P. Gerber, M. Jucker, The building blocks of northern hemisphere wintertime stationary waves. *J. Clim.* **33**(13), 5611–5633 (2020). doi:10.1175/JCLI-D-19-0181.1

57. D. M. Frierson, I. M. Held, P. Zurita-Gotor, A gray-radiation aquaplanet moist GCM. Part I. Static stability and eddy scale. *J. Atmos. Sci.* **63**(10), 2548–2566 (2006). doi:10.1175/JAS3753.1

58. D. M. Frierson, I. M. Held, P. Zurita-Gotor, A gray-radiation aquaplanet moist GCM. Part II. Energy transports in altered climates. *J. Atmos. Sci.* **64**(5), 1680–1693 (2007). doi:10.1175/JAS3913.1

59. T. M. Merlis, T. Schneider, S. Bordoni, I. Eisenman, Hadley circulation response to orbital precession. Part II. Subtropical continent. *J. Clim.* **26**(3), 754–771 (2013).

60. A. K. Betts: A new convective adjustment scheme. Part I: Observational and theoretical basis. *Q. J. R. Meteorolog. Soc.* **112**(473), 677–691 (1986). doi:10.1002/qj.49711247307

61. A. Betts, M. Miller, A new convective adjustment scheme. Part II: Single column tests using GATE wave, BOMES, ATEX and Arctic air-mass data sets. *Q. J. R. Meteorolog. Soc.* **112**(473), 693–709 (1986). doi:10.1002/qj.49711247308

62. E. J. Mlawer, S. J. Taubman, P. D. Brown, M. J. Iacono, S. A. Clough, Radiative transfer for inhomogeneous atmospheres: RRTM, a validated correlated-k model for the longwave. *J. Geophys Res.: Atmos.* **102**(D14), 16,663–16,682, (1997).

63. M. J. Iacono, E. J. Mlawer, S. A. Clough, J.-J. Morcrette, Impact of an improved longwave radiation model, RRTM, on the energy budget and thermodynamic properties of the NCAR community climate model, CCM3. *J. Geophys Res.: Atmos.* 1**05**(D11), 14,873–14,890 (2000).

64. I. P. White, C. G. Garfinkel, E. P. Gerber, M. Jucker, P. Hitchcock, J. Rao, The generic nature of the tropospheric response to sudden stratospheric warmings. *J. Clim.* **33**(13), 5589–5610 (2020).

65. C. I. Garfinkel, I. White, E. P. Gerber, O. Adam, M. Jucker, Nonlinear Interaction between the Drivers of the Monsoon and Summertime Stationary Waves. *Geophys. Res. Lett.*, **48**, (2021) doi:10.1029/2020GL092321.

66. J. Cohen, D. Rind, The effect of snow cover on the climate. *J. Climate*, **4**, 689–706 (1991).

67. H.-M. Kim, B.-M. Kim, Relative contributions of atmospheric energy transport and sea ice loss to the recent warm Arctic winter. *J. Climate*, **30**, 7441–7450, doi:10.1175/JCLI-D-17-0157.1 (2017).

Acknowledgements

Funding

JC is supported by the National Science Foundation grant PLR-1901352.

LA and MB received supported from NSF AGS-1657921 and NOAA NA20OAR4310424.

CIG and IW acknowledge the support of a European Research Council starting grant under the European Union Horizon 2020 research and innovation programme (grant agreement number 677756).

Author contributions:

Conceptualization: JC

Methodology: JC, MB, LA, CIG

Investigation: JC, MB, LA, CIG, IW

Figures: JC, LA, CIG

Supervision: JC

Writing – original draft: JC

Writing – review & editing: JC, MB, LA, CIG, IW

Competing interests: None for all the authors

Data and materials availability: Observational analysis was performed with MERRA2 available at: https://gmao.gsfc.nasa.gov/reanalysis/MERRA-2/. NOAA Snow cover extent is available at: http://climate.rutgers.edu/snowcover/index.php and Arctic sea ice concentration is available at: https://www.metoffice.gov.uk/hadobs/hadisst/.

The version of MiMA used in this study can be downloaded from https://github.com/ianpwhite/MiMA/releases/tag/ MiMA-ThermalForcing-v1.0beta (with DOI: https://doi.org/10.5281/zenodo.4523199). The version of MiMA used in this study follows that used in Garfinkel et al. (*56*) albeit with the albedo and ocean heat-flux modifications as listed in the Methods section. MiMA v2.0 can be downloaded from https://github.com/mjucker/MiMA.

Figure Captions

Fig. 1. Five major patterns of stratospheric polar vortex variability for the months October through December. (**A**) 100-hPa geopotential height composites (contours in 20-dam intervals, anomalies shaded, and 1580-dam contour bolded) for pattern days P1–P5. Percent of days assigned to the pattern is indicated in parentheses. (**B**) Yearly frequency of (left to right) P1–P5 pattern days (grey bars), with dashed lines showing linear trend (blue if statistically significant negative trend, red if significant positive trend, and black otherwise). Statistical significance is at the 0.05 level, as determined by the Wald test with t-distribution of the test statistic. Composites for (left to right) P1–P5 pattern days of **(C)** 500-hPa geopotential heights (in decameters, with anomalies shaded and 540-dam contour bolded), **(D)** mean sea-level pressure anomalies (hPa), and **(E)** 2-m surface temperature anomalies (K). Monthly data are for the years 1980 through 2020.

Fig. 2. Lower-stratospheric and tropospheric precursor patterns to SPV stretching events. Composite fields of (left to right) days 15–11, days 10–6, days 5–1, and day 0 before start of all P4 events for **(A)** 100-hPa geopotential height (dam, contours in 20-dam intervals, anomalies shaded), **(B)** 100-hPa vertical WAF or Plumb flux anomalies (m^2s^{-2}, positive values are upward), **(C)** 500-hPa geopotential height (dam, contours, with anomalies shaded), **(D)** mean sea-level pressure anomalies (hPa), and **(E)** 2-m surface temperature anomalies (K). P4 events are defined as one or more consecutive P4 days. Stippling indicates regions where precursor composite is statistically significant at the .05 level based on random sampling from a full set of days Oct–Dec 1980–2020, using a sample size equal to the number of P4 events.

Fig. 3. Lower-stratospheric and tropospheric trends in late fall and early winter project onto SPV stretching precursors. (**A**) Trends in (left to right) 100-hPa geopotential heights (mdecade^{-1}),100-hPa vertical WAF or Plumb flux (m^2s^{-2} decade^{-1}), 500-hPa geopotential heights (mdecade^{-1}), mean sea-level pressure (hPa decade^{-1}), and 2-m surface temperature (K decade^{-1}) for the period Nov–Feb 1980–2021. (**B**) Correlation between detrended October Eurasian snow cover extent and same fields as in (A) but for Nov-Jan 1980-2021. (**C**) Correlation between detrended Oct-Dec Barents-Kara sea ice concentration and same fields as in (A) but for Dec-Feb 1980-2021. For all panels, stippling indicates regions with statistical significance at the .05 level based on the t-distribution.

Fig. 4. The atmospheric response to a model forced with increased snow cover and sea ice loss resembles atmospheric anomalies associated with SPV stretching events. (**A**) Linear regression using observations between detrended October Eurasian snow cover extent with (top to bottom) detrended 100-hPa geopotential heights (m), 100-hPa meridional heat transport (K ms^{-1}), 500-hPa geopotential heights (m), and 850-hPa temperature (K) for Dec–Feb 1980–2021. (**B**) Composite difference between control run and snow forcing for (left to right) days 76–80 and 81–85 after model initialization of (top to bottom) 100-hPa geopotential height (m), 100-hPa meridional heat transport (K ms^{-1}), 500-hPa geopotential height (m), and 850-hPa temperature (K). (**C**) Multi-linear regression (regression using multiple predictors) using observations between detrended October Eurasian snow cover extent and Oct-Dec Barents-Kara sea ice concentration with for same fields as in (A). (**D**) Composite difference between control run and both Barents-

Kara sea ice and Eurasian snow forcing for (left to right) days 36–40 and 41–45 days after model initialization of the (top to bottom) same fields as in (B). Stippling in (B) and (D) indicates regions with statistical significance at the .05 level based on the t-distribution. For (A–D), 100- and 500-hPa geopotential height panels also show contours of the full field.

Supplementary Materials:

Materials and Methods

References (*44-67*)

Figures S1 to S16

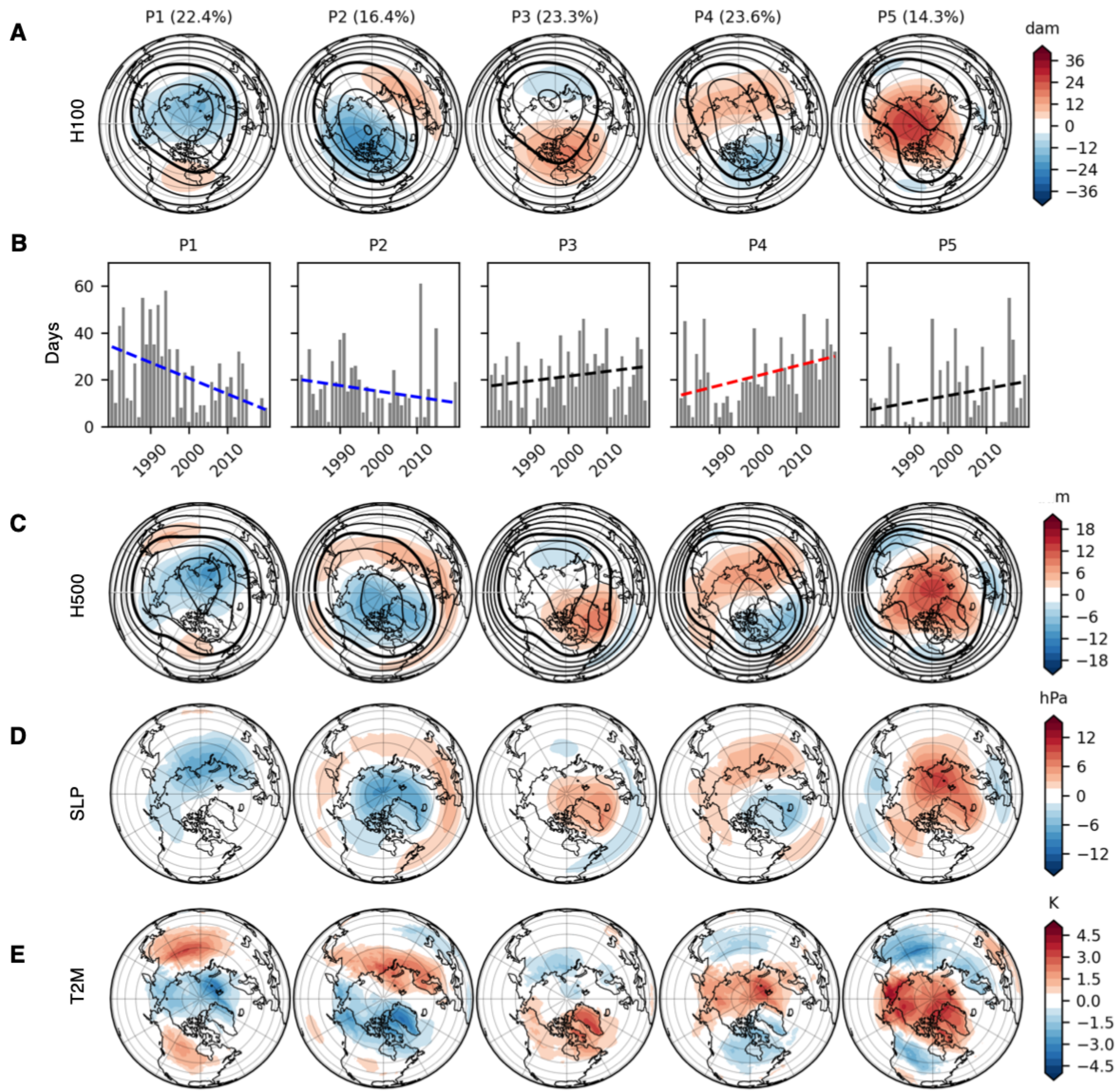
A
B
C
D
E
P1 (22.4%)
P2 (16.4%)
P3 (23.3%)
P4 (23.6%)
P5 (14.3%)
H100
dam
36
24
12
0
−12
−24
−36
P1
P2
P3
P4
P5
Days
0
20
40
60
1990
2000
2010
H500
m
18
12
6
0
−6
−12
−18
SLP
hPa
12
6
0
−6
−12
T2M
K
4.5
3.0
1.5
0.0
−1.5
−3.0
−4.5

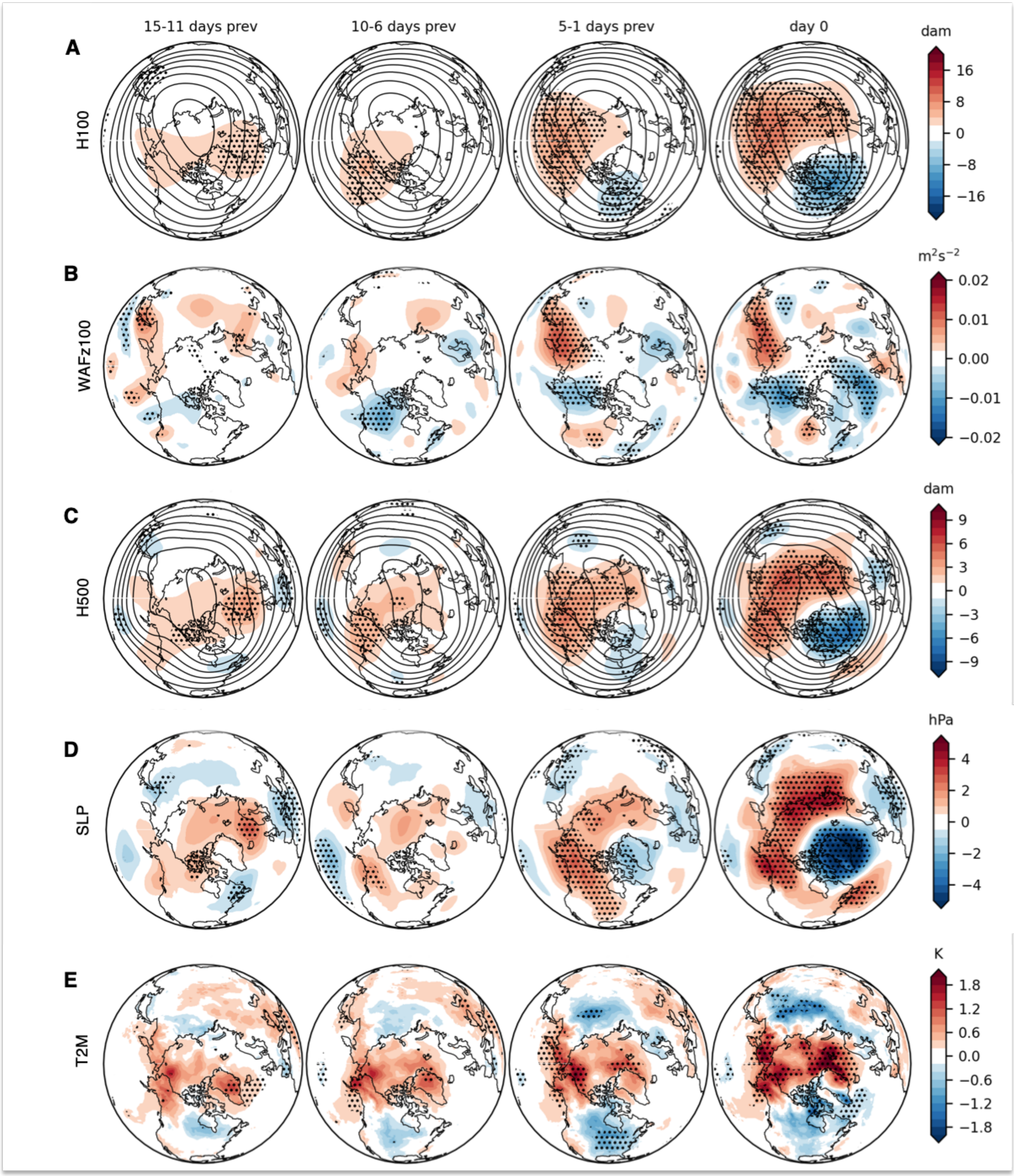

15-11 days prev
10-6 days prev
5-1 days prev
day 0
A
H100
dam
16
8
0
−8
−16
B
WAFz100
m^2s^{-2}
0.02
0.01
0.00
−0.01
−0.02
C
H500
dam
9
6
3
0
−3
−6
−9
D
SLP
hPa
4
2
0
−2
−4
E
T2M
K
1.8
1.2
0.6
0.0
−0.6
−1.2
−1.8

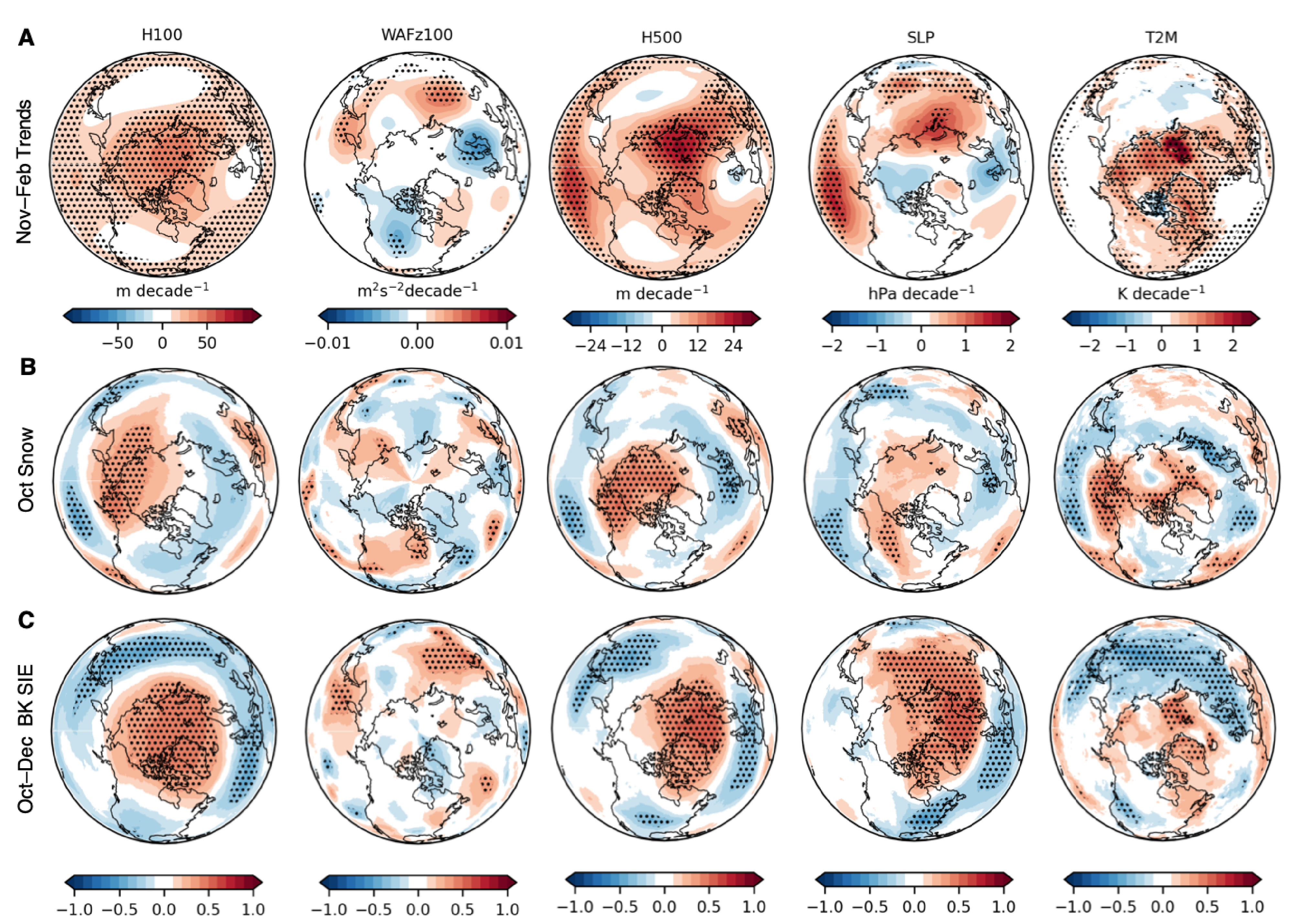

A
H100
WAFz100
H500
SLP
T2M
Nov–Feb Trends
m decade^{-1}
−50 0 50
m^{2}s^{-2}decade^{-1}
−0.01 0.00 0.01
m decade^{-1}
−24 −12 0 12 24
hPa decade^{-1}
−2 −1 0 1 2
K decade^{-1}
−2 −1 0 1 2
B
Oct Snow
C
Oct–Dec BK SIE
−1.0 −0.5 0.0 0.5 1.0

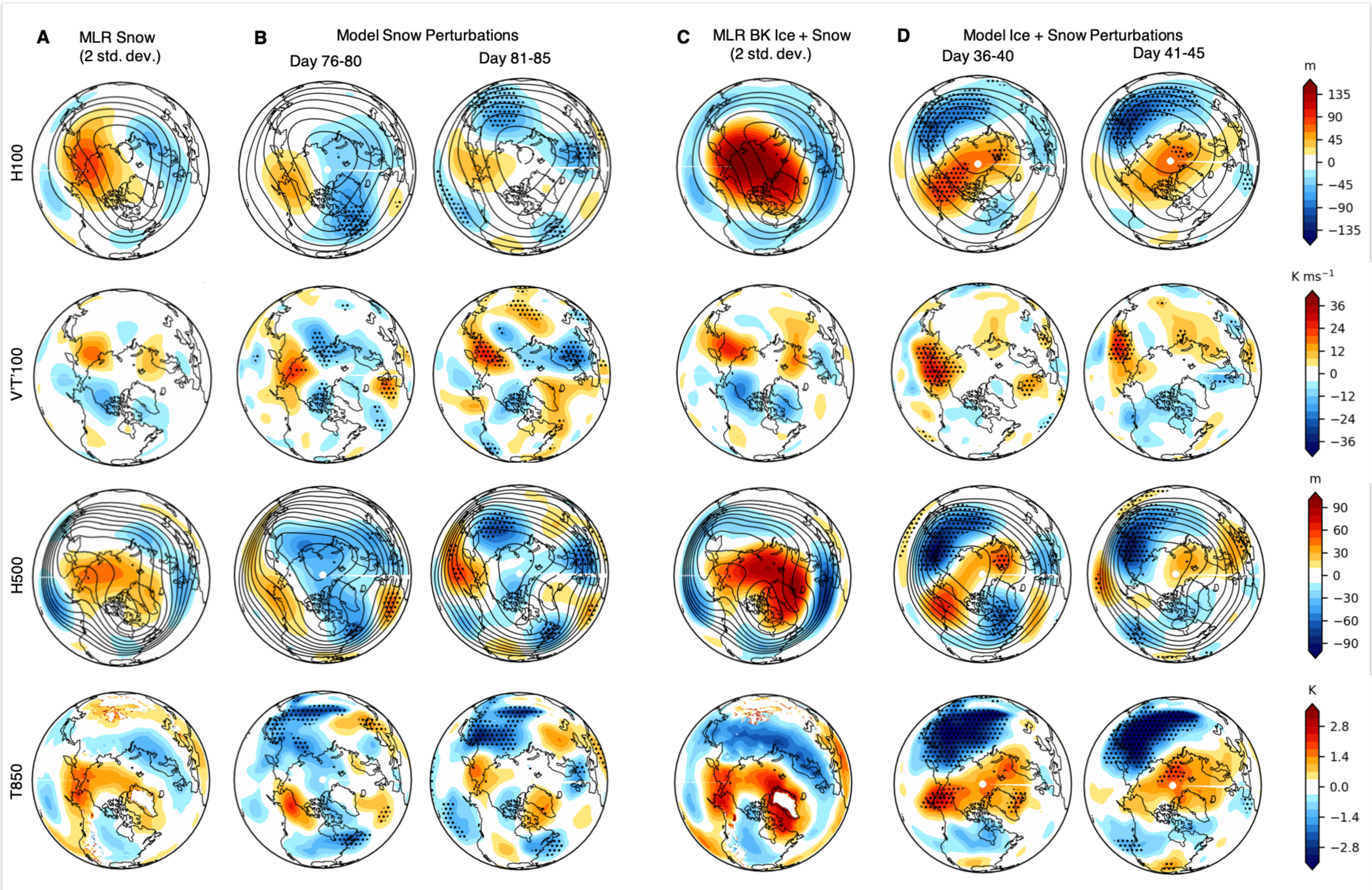

A
MLR Snow
(2 std. dev.)
B
Model Snow Perturbations
Day 76-80
Day 81-85
C
MLR BK Ice + Snow
(2 std. dev.)
D
Model Ice + Snow Perturbations
Day 36-40
Day 41-45
H100
V'T'100
H500
T850
m
135
90
45
0
−45
−90
−135
K ms^{-1}
36
24
12
0
−12
−24
−36
m
90
60
30
0
−30
−60
−90
K
2.8
1.4
0.0
−1.4
−2.8